ACS Catalysis

pubs.acs.org/acscatalysis

Research Article

ZrO_2-Promoted Cu-Co, Cu-Fe and Co-Fe Catalysts for Higher Alcohol Synthesis

Yuzhen Ge, Tangsheng Zou, Antonio J. Martín, and Javier Pérez-Ramírez*

Cite This: *ACS Catal.* 2023, 13, 9946−9959

Read Online

ACCESS | Metrics & More | Article Recommendations | Supporting Information

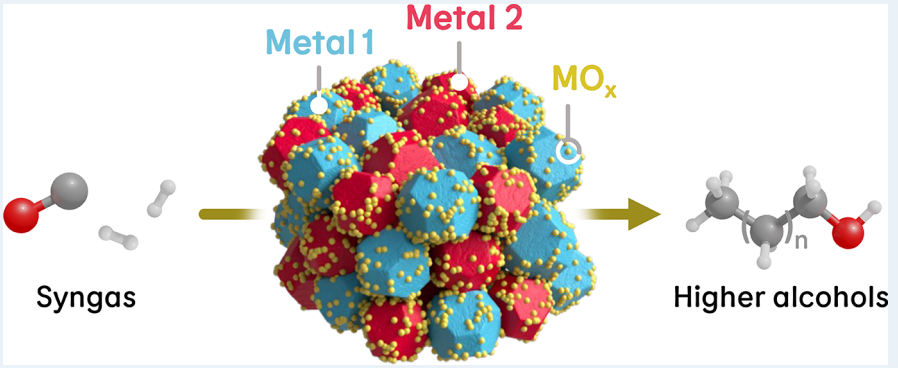

ABSTRACT: The development of efficient catalysts for the direct synthesis of higher alcohols (HA) via CO hydrogenation has remained a prominent research challenge. While modified Fischer−Tropsch synthesis (m-FTS) systems hold great potential, they often retain limited active site density under operating conditions for industrially relevant performance. Aimed at improving existing catalyst architectures, this study investigates the impact of highly dispersed metal oxides of Co-Cu, Cu-Fe, and Co-Fe m-FTS systems and demonstrates the viability of ZrO_2 as a general promoter in the direct synthesis of HA from syngas. A volcano-like composition-performance relationship, in which 5−10 mol % ZrO_2 resulted in maximal HA productivity, governs all catalyst families. The promotional effect resulted in a 2.5-fold increase in HA productivity for the optimized Cu_1Co_4@ZrO_2-5 catalyst (Cu:Co = 1:4, 5 mol % ZrO_2) compared to its ZrO_2-free counterpart and placed Co_1Fe_4@ZrO_2-10 among the most productive systems (345 mg_{HA} h^{-1} g_{cat}^{-1}) reported in this category under comparable operating conditions, with stable performance for at least 300 h. ZrO_2 assumes an amorphous and defective nature on the catalysts, leading to enhanced H_2 and CO activation, facilitated formation of metallic and carbide phases, and structural stabilization.

KEYWORDS: *higher alcohol synthesis, CO hydrogenation, modified Fischer−Tropsch catalysts, Cu-Co, Cu-Fe, Co-Fe, zirconia, promotion*

INTRODUCTION

Higher alcohols (HA) have a large economic value as important building blocks in the chemical, pharmaceutical and energy sectors.[1−3] Currently, the majority of HA are produced by sugar fermentation (ethanol and isobutanol) or by hydration of petroleum-derived alkenes (heavier alcohols).[4,5] The direct synthesis of HA from carbon oxides (CO_2 or CO_2-derived CO) and green hydrogen would present a sustainable and desirable alternative, considering the urgent need to reduce atmospheric CO_2 concentrations.[6]

Research on direct synthesis of HA from syngas (CO + H_2) has been steadily gaining momentum, with the general reaction mechanism regarded as a combination of Fischer−Tropsch synthesis (FTS) and methanol synthesis (MS) steps occurring over distinct sites.[7−9] CO is dissociatively adsorbed on FTS functionalities forming C_nH_x* species for carbon chain growth (C-C coupling), and nondissociatively adsorbed on MS ones as CO*, which may be hydrogenated to form CHO* species.[10−13] Critically, the coupling of C_nH_x* with CO*/CHO* species (CO insertion) to form C_nH_xCO*, and subsequently the alcohol, necessitates a well-balanced population of both types of sites in close proximity.[14] Metallic copper is well-known for its high activity in MS and hydrogenation ability, whereas cobalt and iron are reference metals for FTS, as their carbide phases are known to be active for carbon chain growth.[10,11] Cu-Co and Cu-Fe-based systems have thus been investigated for HA synthesis from syngas as they integrate both functionalities.[15−18] In these catalysts, HA productivity is indeed tightly linked to a high interfacial

Received: June 4, 2023
Revised: June 30, 2023
Published: July 14, 2023

https://doi.org/10.1021/acscatal.3c02534
ACS Catal. 2023, 13, 9946−9959

density.[19] However, the low solubility of Cu in Co and Fe (<10 at. %, based on bimetallic phase diagrams[19,20]) usually causes severe dealloying and sintering under reaction conditions[21] for catalysts exclusively formed by the two metals (labeled as $M_{1\alpha}M_{2\beta}$, with α:β denoting the molar metal ratio, Figure 1). Families with enhanced solubility between metals

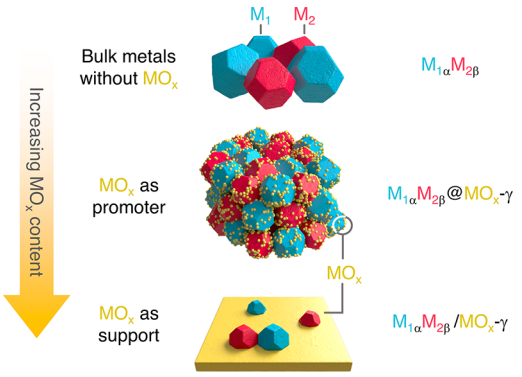

Figure 1. Catalyst architectures for bimetallic M_1M_2 catalysts containing a variable fraction of a metal oxide (MO_x) of either zero, a small, or the largest fraction. α:β represents the molar M_1:M_2 ratio and γ the molar content of metal oxide.

like the Co-Fe system have also been explored, with the belief that the MS functionality is provided by Co carbides formed during operation.[22] In this case, performance is still limited by the sintering of active metals, reducing the density of surface sites.

The most commonly adopted strategy is the deposition of nanoparticulated M_1M_2 on supports with confined porous nanostructures like zeolitic imidazolate frameworks, carbon nanotubes, or on high-surface area carriers, such as active carbon, layered double hydroxides, and certain metal oxides (MO_x, oxide-supported catalysts denoted as $M_{1\alpha}M_{2\beta}/MO_x$, Figure 1). Interactions between oxide supports and active metal nanoparticles do not only stabilize the latter, but could also induce surface reconstruction or confer promotional qualities for intermediate formation in HAS, among other general effects of structural and electronic nature.[17,23,24] Increased dispersion or confinement of M_1M_2 particles by large amounts of bulk MO_x tends to reduce the degree of sintering at the expense of a modest density of interfacial active sites. More recently, reversing the traditional catalyst architecture by dispersing the metal oxide (typically <20% of the total composition) on the surface of active metals has created alternative configurations with increased interfacial site densities[25−27] with promise mostly in model surfaces for relatively simple reactions such as CO and CO_2 methanation, CO oxidation, water−gas shift and methanol synthesis.[28−30]

Inspired by these developments, we explore the potential of using relatively low quantities of highly dispersed metal oxides on the surface of bimetallic m-FTS catalysts (denoted by $M_{1\alpha}M_{2\beta}@MO_x$-$\gamma$, where γ represents the molar MO_x content, Figure 1) as promoters in HAS. This research was first developed for the most widely studied Co-Cu family and later generalized to Cu-Fe and Co-Fe systems. Following the development of a dedicated sol−gel synthesis strategy targeting the desired architectures, the evaluation of various metal oxides recommended ZrO_2 for further studies toward optimized compositions in all cases. As a result, the best ZrO_2-promoted $M_{1\alpha}M_{2\beta}@ZrO_2$-10 catalyst outperformed its unpromoted $M_{1\alpha}M_{2\beta}$ and ZrO_2-supported $M_{1\alpha}M_{2\beta}$ counterparts, exhibiting no clear sign of deactivation for at least 300 h on stream. Characterization efforts disclosed the amorphous and defective nature of ZrO_2 and its promotional role. Beyond increasing surface area and structural stability, ZrO_2 favors the evolution of metal species toward metallic and cobalt carbide forms, enabling more facile activation of H_2 and CO.

EXPERIMENTAL SECTION

Catalyst Preparation. $M_{1\alpha}M_{2\beta}@MO_x$-$\gamma$ catalysts with molar M_1:M_2 ratios of α:β and MO_x contents of γ mol % (based on metals) were prepared via a sol−gel method[4,30,31] (Figure 2). Appropriate amounts of metal precursors [$Cu(NO_3)_2{\cdot}3H_2O$ (Sigma-Aldrich, 98%), $Co(NO_3)_2{\cdot}6H_2O$ (Sigma-Aldrich, 98%), $Fe(NO_3)_3{\cdot}9H_2O$ (Sigma-Aldrich, 98%), and one of $ZrO(NO_3)_2{\cdot}3H_2O$ (Acros Organics, 99.5%), $Mg(NO_3)_2{\cdot}6H_2O$ (Sigma-Aldrich, 99%), $Al(NO_3)_3{\cdot}9H_2O$ (Acros Organics, 99%), $Al(NO_3)_2)_2{\cdot}4H_2O$ (Alfa Aesar, 98%), $Zn(NO_3)_2{\cdot}6H_2O$ (Acros Organics, 98%) or $Ce(NO_3)_3{\cdot}6H_2O$ (Acros Organics, 99%)] required for a total concentration of 1 M with the targeted nominal metal contents were dissolved in 100 mL of ethanol (Fisher Scientific, 99.8%). For $Cu_\alpha Co_\beta@MO_x$-γ, a 100 mL solution of 2 M oxalic acid (Acros Organics, 98%) in ethanol was added dropwise to the metal precursor solution under vigorous stirring (500 rpm) for 30 min at room temperature. The resulting gel containing a metal-oxalate complex was separated from excess solvent by centrifugation (6000 rpm for 10 min) and washed with 150 mL of ethanol twice. For $Cu_\alpha Fe_\beta@MO_x$-γ and $Co_\alpha Fe_\beta@MO_x$-γ, a 100 mL solution of 2 M L-(+)-tartaric acid (Sigma-Aldrich, 99%) in ethanol was added dropwise to the metal precursor solution under vigorous stirring (500 rpm) for 12 h at room temperature. The resulting gel containing a metal-tartrate complex was separated from excess solvent by rotary evaporation using a Büchi Rotavapor R-114 instrument at 323 K and 50 mbar. The colloids obtained were dried in a vacuum oven at 373 K for 12 h and calcined in static air at 673 K (heating rate = 2 K min^{-1}) for 3 h.

Figure 2. Sol−gel synthesis procedure developed for $M_{1\alpha}M_{2\beta}@MO_x$-$\gamma$ catalysts. Synthesis steps are detailed in the Experimental Section.

https://doi.org/10.1021/acscatal.3c02534
ACS Catal. 2023, 13, 9946−9959

ZrO_2-supported $M_{1\alpha}M_{2\beta}$ catalysts were prepared by wet impregnation. An aqueous solution containing appropriate amounts of $Cu(NO_3)_2{\cdot}3H_2O$, $Co(NO_3)_2{\cdot}6H_2O$ and/or $Fe(NO_3)_3{\cdot}9H_2O$ was added dropwise to ZrO_2 powder (Alfa Aesar, 99%) at room temperature under stirring for 6 h. The resultant solid was dried in a vacuum oven at 373 K for 12 h and calcined in static air at 673 K (2 K min^{-1}) for 3 h.

Catalyst Characterization. X-ray fluorescence spectroscopy (XRF) was performed by using an Orbis Micro-EDXRF spectrometer equipped with a Rh source operated at 35 kV and 500 μA and a silicon drift detector.

Nitrogen sorption was carried out using a Micromeritics TriStar II physisorber employing the Brunauer−Emmett−Teller (BET) method to calculate the surface area. Prior to the measurements, samples were degassed under vacuum (10 Pa) at 473 K for 4 h.

X-ray diffraction (XRD) was conducted using a Rigaku SmartLab diffractometer with a D/teX Ultra 250 detector using Cu Kα radiation (λ = 0.1541 nm) and operating in a Bragg−Brentano geometry. Data were acquired in the 5−80° 2θ range with an angular step size of 0.025° and a counting time of 1.5 s per step.

Temperature-programmed reduction with hydrogen (H_2-TPR) was performed at ambient pressure using a Micromeritics AutoChem HP II analyzer. Samples were loaded into a quartz tube, dried at 423 K in Ar for 1 h (10 K min^{-1}), and cooled to 313 K (20 K min^{-1}) in Ar. The temperature-programmed reduction was then carried out using 5 vol % H_2 in N_2 (Messer) and increasing the temperature to 1073 K (5 K min^{-1}) with H_2 consumption quantified by a thermal conductivity detector (TCD).

Temperature-programmed desorption of CO (CO-TPD) was performed by using a Micromeritics AutoChem HP II analyzer coupled to a Pfeiffer OMNIStar mass spectrometer (MS). Samples were loaded into a quartz tube, exposed to 5 vol % H_2 in Ar at 623 K (5 K min^{-1}) for 4 h to ensure complete surface reduction, and then flushed with Ar. Adsorption of CO was carried out using 5 vol % CO in He at 313 K for 1 h, followed by flushing with Ar for 30 min. The temperature-programmed desorption was then conducted in Ar and the temperature was increased to 973 K (5 K min^{-1}).

Temperature-programmed H_2-D_2 exchange was performed using a Micromeritics AutoChem HP II analyzer coupled to a Pfeiffer OMNIStar MS. Used samples were loaded into a quartz tube, dried at 423 K in Ar for 1 h (10 K min^{-1}), and cooled to 313 K (20 K min^{-1}) in Ar. The H_2-D_2 exchange reaction was then carried out under 5 vol % D_2 (Sigma-Aldrich, 99.8%) and 5 vol % H_2 in N_2 (Messer) and increasing the temperature to 873 K (5 K min^{-1}), with the outlet flow of H_2, D_2 and HD quantified by online MS.

High-resolution transmission electron microscopy (HRTEM) and high-angle annular dark-field scanning transmission electron microscopy (HAADF-STEM) images were collected using an aberration-corrected JEM-ARM300F microscope (GrandARM, JEOL) operated at 300 kV and a Talos F200X instrument operated at an acceleration potential of 200 kV, respectively. Energy-dispersive X-ray (EDX) spectroscopy and elemental mapping were carried out using a Talos instrument equipped with four silicon drift detectors (SDD).

X-ray photoelectron spectroscopy (XPS) was performed using a Physical Electronics (PHI) Quantum 2000 X-ray photoelectron spectrometer featuring monochromatic Al Kα radiation, generated from an electron beam operated at 15 kV and 32.3 W and a hemispherical capacitor electron-energy analyzer equipped with a channel plate and a position-sensitive detector. Analyses were conducted at 2 × 10^{-7} Pa, with an electron takeoff angle of 45°, operating the analyzer in the constant pass energy mode. The energy scale of the instrument was calibrated using Au and Cu as reference samples.

Catalyst Evaluation. A continuous-flow fixed-bed reactor setup described in detail elsewhere[32,33] was used for the direct conversion of syngas to HA. Sieved powder catalyst between 0.3 and 0.6 mm in particle size was diluted by twice the catalyst mass of quartz sand and loaded into the reactor. Prior to catalyst activation, a leak test was conducted by increasing the pressure to 5 MPa under an Ar (Messer, purity 5.0) flow. The catalyst was activated in situ in dilute hydrogen to reduce surface metal oxides, under a 40 cm^3 min^{-1} flow of 50 vol % H_2 (Messer, purity 5.0) in Ar at atmospheric pressure and a temperature of 623 K (5 K min^{-1}) for 4 h. After the reactor was cooled to the reaction temperature (T) and pressurized to the reaction pressure (P) under Ar flow, the reaction mixture of CO (Messer, purity 5.0), H_2, and Ar was fed into the reactor. The standard reaction and feed conditions that were selected for catalyst screening were T = 543 K, P = 5 MPa, and $GHSV$ = 24000 cm^3 h^{-1} g_{cat}^{-1} with a molar ratio of H_2:CO:Ar = 6:3:1. Kinetic investigations were additionally conducted in the ranges of T = 473−573 K, P = 3−7 MPa, H_2:CO = 1−3, and $GHSV$ = 6000−48000 cm^3 h^{-1} g_{cat}^{-1}. The outlet stream was sampled every 1 h and analyzed online by gas chromatography (GC, Agilent 6890A), with calculations performed taking average values of 3 measurements between ca. 14 and 16 h on stream.

The CO conversion (X_{CO}) was calculated using eq 1:

$$X_{CO} = \frac{n_{CO,in} - n_{CO,out}}{n_{CO,in}} \quad (1)$$

where $n_{CO,in}$ and $n_{CO,out}$ are the inlet and outlet CO molar flows, respectively.

The selectivity for product i (S_i) was calculated using eq 2:

$$S_i = \frac{n_{i,out} \times N_{C,i}}{\sum (n_{i,out} \times N_{C,i})} \times 100\% \quad (2)$$

where $n_{i,out}$ and $N_{C,i}$ are the molar flow and the number of carbon atoms in product i, respectively. The selectivity to HA and hydrocarbons was obtained by summing the individual selectivity to alcohols and hydrocarbons with 2 or more carbon atoms.

The space time yield of HA (STY_{HA}) expressed in mg_{HA} h^{-1} g_{cat}^{-1} was calculated using eq 3:

$$STY_{HA} = \sum S_{j,HA} \times MW_{j,HA} \times \frac{X_{CO} \times n_{CO,in}}{m_{cat}} \quad (3)$$

where m_{cat} is the mass of the catalyst and $MW_{j,HA}$ is the molecular weight of higher alcohols containing j carbon atoms. Despite the disparity in the number of active sites between the catalysts of different architectures and the current unfeasibility of its quantification, a practically relevant comparison could be made by normalizing HA productivity in terms of STY_{HA} by catalyst mass.

The carbon balance (δ_C) was determined according to eq 4 and showed always less than a 10% difference between the reactant and product streams:

https://doi.org/10.1021/acscatal.3c02534
ACS Catal. 2023, 13, 9946−9959

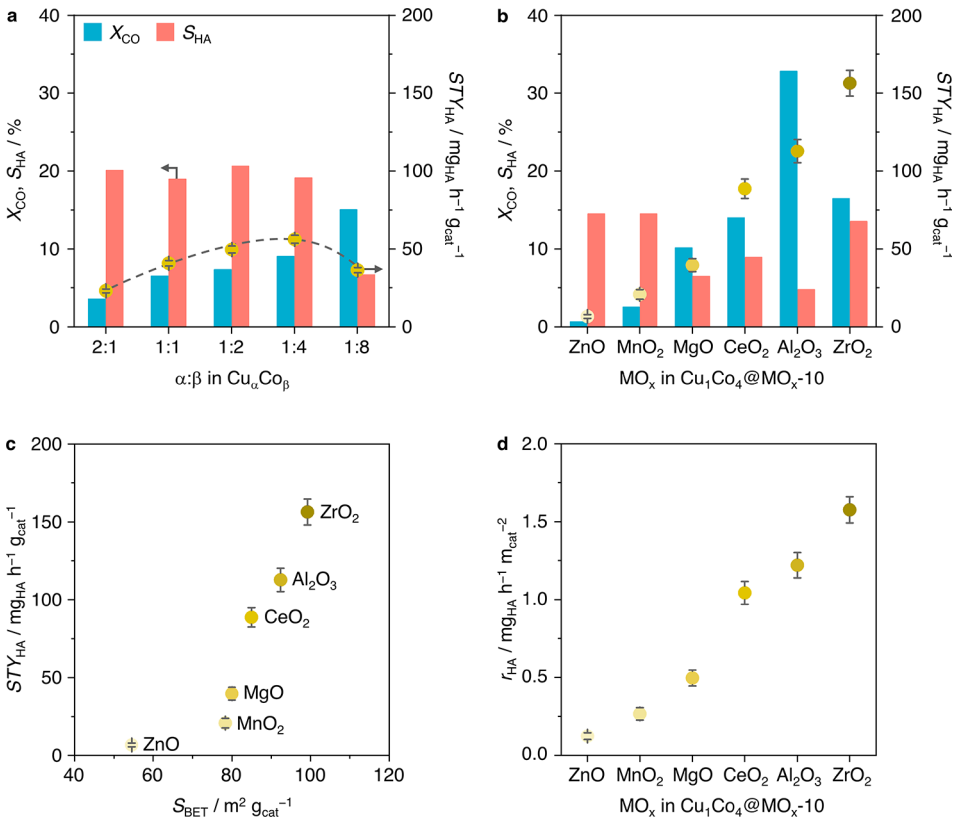

Figure 3. (a) Influence of the α:β ratio on catalytic performance for $Cu_\alpha Co_\beta$ catalysts. Reaction conditions: T = 543 K, P = 5.0 MPa, and H_2:CO = 2.0. $GHSV$ = 12000 cm^3 h^{-1} g_{cat}^{-1}. Influence of MO_x on (b) catalytic performance, (c) the relation between STY_{HA} and S_{BET}, and (d) STY_{HA} normalized by S_{BET} (r_{HA}) for Cu_1Co_4@MO_x-10 catalysts. Reaction conditions: T = 543 K, P = 5.0 MPa, H_2:CO = 2.0, $GHSV$ = 24000 cm^3 h^{-1} g_{cat}^{-1}. Error bars representing the standard deviation of 3 measurements at TOS between 14 and 16 h are shown. Trend lines are added to guide the eye.

$$\delta_C = \frac{n_{CO,in} - \sum n_{i,out} \times N_{C,i}}{n_{CO,in}} \times 100\% \quad (4)$$

RESULTS AND DISCUSSION

Basic Properties of $M_{1\alpha}M_{2\beta}$@MO_x-γ. $M_{1\alpha}M_{2\beta}$@MO_x-γ catalysts were synthesized via a sol−gel method (Experimental Section and Figure 2) which allowed both active metal centers to be chelated by dicarboxylate ion ligands in a polymeric network with an even metallic distribution.[31] Pre-catalysts after calcination in air consisted of a mixture of metal oxides (Figure S1) with general properties detailed in Tables S1−S3. Molar contents measured by XRF coincided within small variance with nominal values, confirming the absence of metal leaching during synthesis.

Impact of MO_x Identity for $Cu_\alpha Co_\beta$@MO_x-γ Systems. To simplify the discussion of performance trends for all three families, the most widely studied Co-Cu combination is first developed and later generalized to Cu-Fe and Co-Fe systems. The identification of metal oxides with potential to act as promoters was developed using the optimal α:β ratio for $Cu_\alpha Co_\beta$ catalysts. For this, the performance of $Cu_\alpha Co_\beta$ catalysts with variable α:β was first evaluated in the direct conversion of syngas to HA at T = 543 K, P = 5.0 MPa, and molar H_2:CO = 2.0 (Figure 3a and Table S4). CO conversion increased linearly with the increasing Co content as dissociative adsorption and activation of CO are enhanced, with STY_{HA} peaking at 56 mg_{HA} h^{-1} g_{cat}^{-1} for Cu_1Co_4, before the population of Cu sites expectedly becomes insufficient to keep supporting performance gains.

Upon selection of the optimal α:β = 1:4, catalysts with 10 mol % metal oxide content (Cu_1Co_4@MO_x-10) were prepared and evaluated. Metal oxides including ZnO, MnO_2, MgO, CeO_2, ZrO_2 and Al_2O_3 were selected based on their broad range of reducibility and acid−base properties. The analysis of catalytic performance (Figure 3b and Table S5) suggests two groups: ZnO, MnO_2, and MgO yielded lower X_{CO} and STY_{HA} values than MO_x-free Cu_1Co_4, whereas CeO_2, ZrO_2, and Al_2O_3 provide superior ones. Apart from the methanol-favoring Cu_1Co_4@ZnO-10 catalyst, overall product distributions were similar for the other MO_x, exhibiting selectivities toward HA between 5 and 15% and selectivities toward hydrocarbons, the major set of byproducts, generally exceeding 80%. CO conversion follows ZnO < MnO_2 < MgO < (Cu_1Co_4) < CeO_2 < ZrO_2 < Al_2O_3. Since the outstanding X_{CO} over Cu_1Co_4@Al_2O_3-10 does not reflect a similarly high STY_{HA} due to its low S_{HA}, Cu_1Co_4@ZrO_2-10 offered the highest STY_{HA} of 156 mg_{HA} h^{-1} g_{cat}^{-1} in this initial screening arising from its compromise between X_{CO} and S_{HA}.

Basic characterization was performed to investigate the superiority of ZrO_2 over other oxides. HAADF-STEM images with EDX elemental mapping of Cu_1Co_4@MO_x-10 show that Cu, Co, and MO_x were generally highly dispersed in all calcined samples with minor differences (Figure S2), with S_{BET} of all calcined Cu_1Co_4@MO_x-10 samples exceeding that of Cu_1Co_4 (Table S1). The correlation of STY_{HA} with increasing S_{BET} (Figure 3c) and decreasing Co_3O_4 crystallite size (Figure

https://doi.org/10.1021/acscatal.3c02534
ACS Catal. 2023, 13, 9946−9959

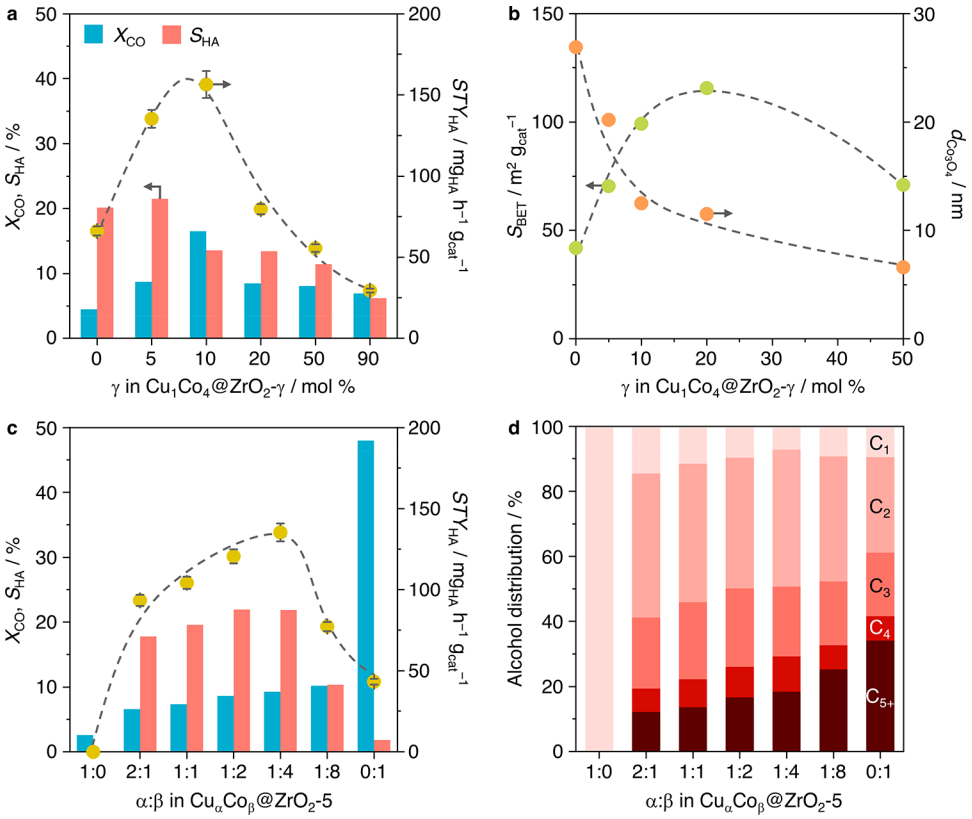

Figure 4. Influence of γ on (a) catalytic performance and (b) S_{BET} and crystallite sizes as determined by XRD analysis for Cu_1Co_4@ZrO_2-γ catalysts. Systems with γ = 0 mol % and γ = 90 mol % are equivalent to Cu_1Co_4 and supported Cu_1Co_4/ZrO_2-90 systems, respectively. Influence of the α/β ratio on (c) catalytic performance and (d) alcohol distribution for $Cu_\alpha Co_\beta$@ZrO_2-5 catalysts. Reaction conditions: T = 543 K, P = 5.0 MPa, H_2:CO = 2.0, $GHSV$ = 24000 cm^3 h^{-1} g_{cat}^{-1}. Error bars representing the standard deviation of 3 measurements at TOS between 14 and 16 h are shown. Trend lines are added to guide the eye.

S3 and Table S1) points to the notable role of the oxide in the inverse architecture as a geometric spacer fostering the formation of smaller Cu and Co oxide nanoparticles. Next, we investigated whether this effect can entirely account for trends in catalytic performance. Indeed, normalization of STY_{HA} by S_{BET} (r_{HA}) strongly suggested other effects at play beyond geometric ones dependent on the identity of MO_x that are likely electronic and interfacial in nature (Figure 3d). After these results, the $Cu_\alpha Co_\beta$@ZrO_2-γ family was selected for further investigation.

Composition-Performance Trends for $Cu_\alpha Co_\beta$@ZrO_2-γ Systems. The influence of ZrO_2 content as well as Cu:Co ratio on catalytic performance was studied to uncover composition-performance trends shaping $Cu_\alpha Co_\beta$@ZrO_2-γ systems. The impact of the ZrO_2 content on catalytic performance was first evaluated, revealing distinct volcano relationships in both X_{CO} and STY_{HA} with maxima at γ = 10 mol % ZrO_2 (Figure 4a and Table S6). HA productivity was 2.4 and 5.3−10 times higher than over the unpromoted Cu_1Co_4 catalyst and ZrO_2-rich Cu_1Co_4 catalysts prepared either by traditional wet impregnation on commercial ZrO_2 or by the sol−gel method, respectively. For reference, pure ZrO_2 was prepared by the same sol−gel method and showed no conversion of CO. Figure 4b shows the influence of γ on the BET surface area and crystallite sizes for Cu_1Co_4@ZrO_2-γ systems. Low contents (γ = 5−20 mol %) promote higher BET surface areas and decreased crystallite sizes (Table S1 and Figure S4), which expectedly enhanced the CO conversion and productivity of HA.

The variation of catalytic performance with respect to Cu and Co content was then investigated, with ZrO_2 fixed at 5 mol % ($Cu_\alpha Co_\beta$@ZrO_2-5). A volcano-like relationship between performance and α:β emerged (Figure 4c and Table S7). The monometallic extremes of Cu@ZrO_2-5 and Co@ZrO_2-5 were, as expected, highly selective toward methanol and hydrocarbons, respectively, with negligible HA productivity. Performance largely increased, however, for Cu_1Co_4@ZrO_2-5 (S_{HA} = 21.9%, STY_{HA} = 135 mg_{HA} h^{-1} g_{cat}^{-1}), confirming the optimality of the Cu:Co ratio of 1:4 chosen to identify the best oxide promoter (Figure 3). Values for α:β below the optimal 1:4 resulted in increasing X_{CO} and favored production of C_1 byproducts, namely, CH_4 and CO_2. The alcohol distribution was slightly influenced by α:β (Figure 4d), as the proportion of longer-chained (notably C_{5+}) alcohols increases with the relative Co content, which could be attributed to enhanced dissociative adsorption of CO and the resultant coupling between generated CH_x* species.[34] As the best compromise between high activity and HA selectivity, Cu_1Co_4@ZrO_2-5 was selected for further characterization and kinetic investigations.

The influence of operating temperatures, pressures, molar H_2:CO feed ratios, and $GHSV$ on HAS over the optimal Cu_1Co_4@ZrO_2-5 was systematically explored (Figure 5 and Table S8). An increase in reaction temperature expectedly raised X_{CO} at the expense of S_{HA} (Figure 5a) due to the exothermicity of alcohol formation. Arrhenius plots (Figure S5) gave access to apparent activation energies in the vicinity of 50 kJ mol^{-1} for the formation of methanol, alkenes, and HA, compared to around 80 kJ mol^{-1} for methane and alkane

https://doi.org/10.1021/acscatal.3c02534
ACS Catal. 2023, 13, 9946−9959

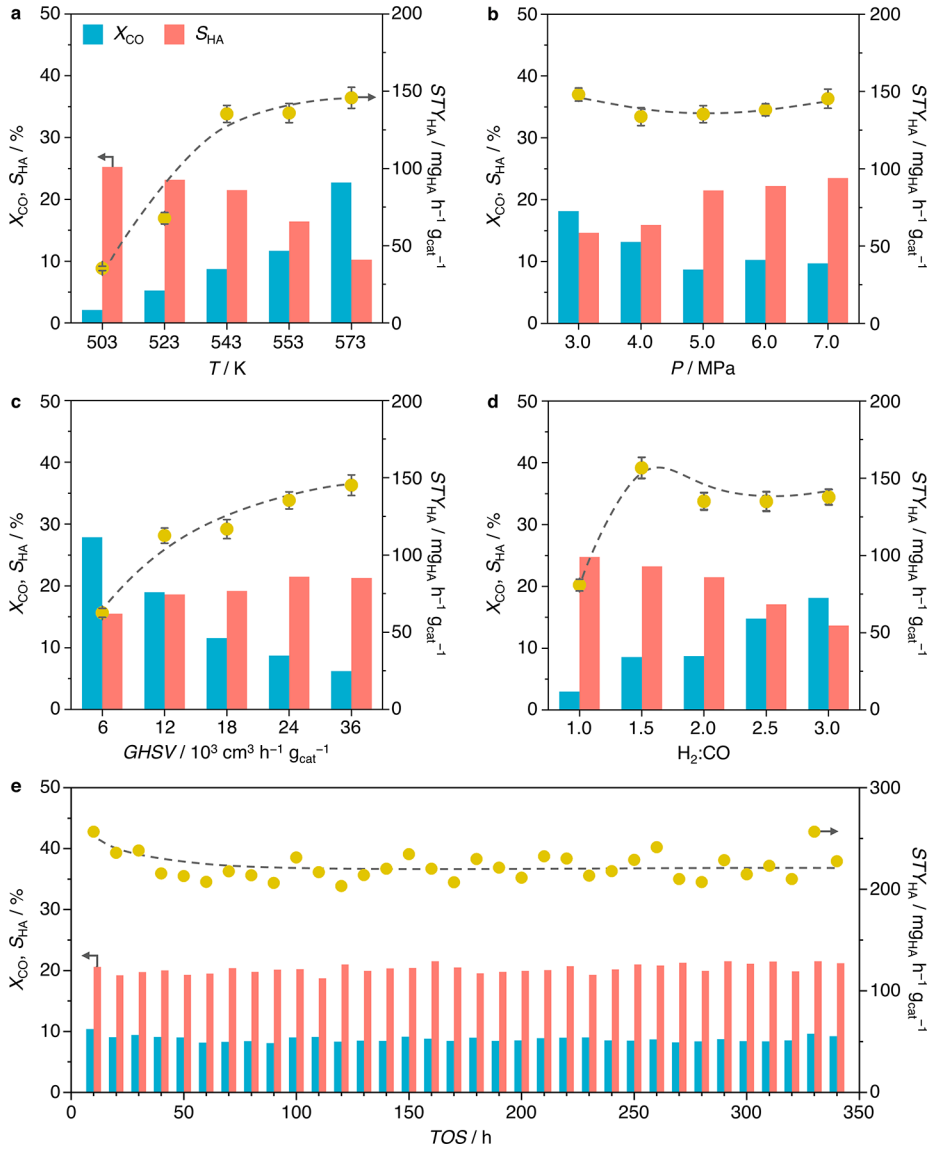

Figure 5. Influence of (a) temperature, (b) pressure, (c) space velocity, and (d) H_2:CO ratio on catalytic performance for the Cu_1Co_4@ZrO_2-5 catalyst. Reaction conditions: T = 543 K, P = 5.0 MPa, H_2:CO = 2, $GHSV$ = 24000 cm^3 h^{-1} g_{cat}^{-1}. Error bars representing the standard deviation of 3 measurements at TOS between 14 and 16 h are shown. (e) Stability test over Cu_1Co_4@ZrO_2-5. Reaction conditions: T = 548 K, P = 5.5 MPa, H_2:CO = 1.5, $GHSV$ = 36000 cm^3 h^{-1} g_{cat}^{-1}. Trend lines are added to guide the eye.

formation. These results were overall lower than those reported for supported Co-Cu catalysts likely due to different reaction conditions.[35] Of note, the decrease in X_{CO} upon increasing total pressure (Figure 5b) seemingly contradicts Le Chatelier's principle and previously reported results,[33] possibly associated with changes in surface H*/CO* coverage or pressure-induced phase and structural evolution.[24] Lowered residence time by increasing $GHSV$ expectedly enhanced S_{HA} at the expense of X_{CO} (Figure 5c), also increasing selectivity toward methanol and alkenes, reducing that toward alkanes. This arguably hints at faster kinetics in CO insertion steps into CH_x* yielding HA than in hydrogenation steps forming alkanes, and decreased residence times favoring desorption of intermediates toward HA formation.[33] Finally, increasing the molar H_2:CO feed ratio enhanced X_{CO} and the selectivity toward paraffins due to the greater availability of H_2, but reduced the selectivity toward methanol and HA[36] (Figure 5d), with low H_2:CO = 1.0−1.5 proving optimal for S_{HA} and STY_{HA}. Exploiting the knowledge gained from this kinetic study, the stability of Cu_1Co_4@ZrO_2-5 was assessed in a 300 h catalytic run under optimized reaction conditions (T = 548 K, P = 5.5 MPa, H_2:CO = 1.5, and $GHSV$ = 36000 cm^3 h^{-1} g_{cat}^{-1}, Figure 5e). A first equilibration period of about 50 h led to stable X_{CO} = 9% and STY_{HA} = 220 mg_{HA} h^{-1} g_{cat}^{-1}. A constant S_{HA} of 21% was kept throughout (Figure S6), showing a lack of apparent catalyst deactivation beyond the initial reaction-induced structural changes.

Composition-Performance Trends for $Cu_\alpha Fe_\beta$@MO_x-γ and $Co_\alpha Fe_\beta$@MO_x-γ Systems. The suitability of ZrO_2 as a promoter also applied to the other two bimetallic catalyst families, namely, $Cu_\alpha Fe_\beta$@MO_x-γ and $Co_\alpha Fe_\beta$@MO_x-γ, given the generally superior performance of the promoted catalysts containing ZrO_2 compared to other MO_x (Tables S9 and S10). An analogous investigation to the case of Cu-Co catalysts for the bimetallic α:β ratio (Figures S7 and S8, Tables S11 and S12) and the ZrO_2 content γ (Figure 6 and Tables S13 and

https://doi.org/10.1021/acscatal.3c02534
ACS Catal. 2023, 13, 9946−9959

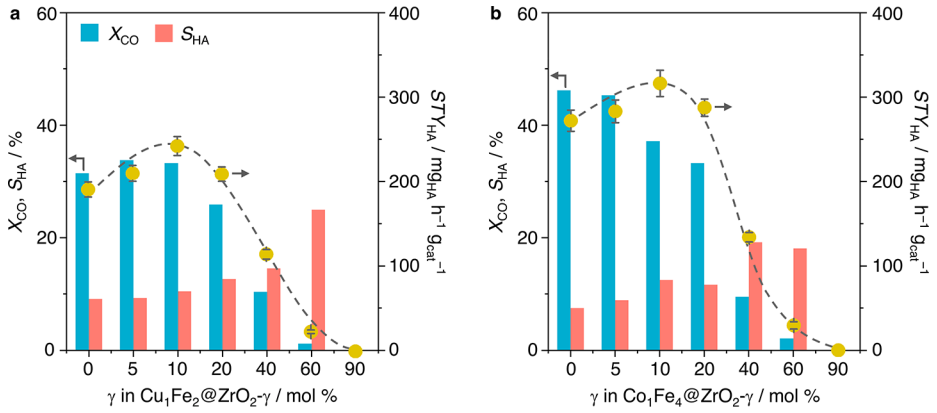

Figure 6. Influence of γ on catalytic performance for (a) Cu_1Fe_2@ZrO_2-γ and (b) Co_1Fe_4@ZrO_2-γ. Reaction conditions: T = 523 K, P = 5.0 MPa, H_2:CO = 2.0, $GHSV$ = 24000 cm^3 h^{-1} g_{cat}^{-1}. Error bars representing the standard deviation of 3 measurements at TOS between 14 and 16 h are shown. Trend lines are added to guide the eye.

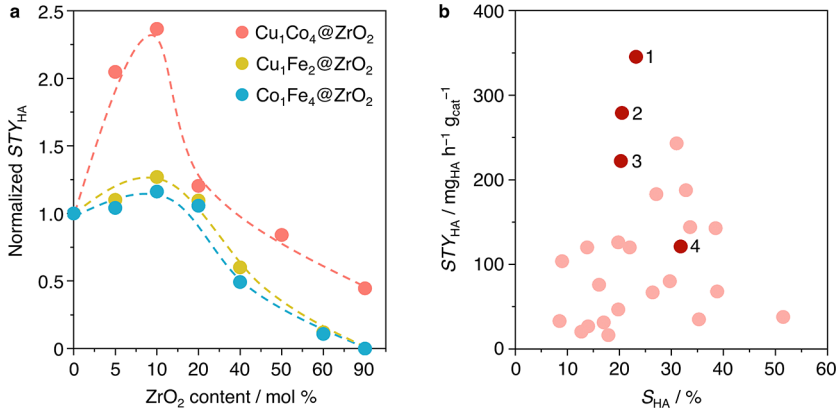

Figure 7. (a) Influence of ZrO_2 content on normalized STY_{HA} for M_1M_2@ZrO_2 catalysts. (b) Comparison of STY_{HA} and S_{HA} of M_1M_2@ZrO_2 catalysts at individually optimized reaction conditions with those of representative m-FTS catalysts previously reported in the literature (Table S17). (1) Co_1Fe_4@ZrO_2-10, reaction conditions: T = 518 K, P = 5.5 MPa, H_2:CO = 1.5, and $GHSV$ = 48000 cm^3 h^{-1} g_{cat}^{-1}. (2) Cu_1Fe_2@ZrO_2-10, reaction conditions: T = 503 K, P = 5.5 MPa, H_2:CO = 1.5, $GHSV$ = 36000 cm^3 h^{-1} g_{cat}^{-1}. (3) Cu_1Co_4@ZrO_2-5, reaction conditions: T = 548 K, P = 5.5 MPa, H_2:CO = 1.5, $GHSV$ = 36000 cm^3 h^{-1} g_{cat}^{-1}. (4) Co_1Fe_4@ZrO_2-10, reaction conditions: T = 473 K, P = 5.0 MPa, H_2:CO = 2.0, $GHSV$ = 24000 cm^3 h^{-1} g_{cat}^{-1}.

S14) revealed Cu_1Fe_2@ZrO_2-10 and Co_1Fe_4@ZrO_2-10 as the best performers in their respective families. Given the higher catalytic performance of the Cu_1Fe_2 and Co_1Fe_4 catalysts, however, the relative improvement in STY_{HA} provided by the addition of ZrO_2 is not as extreme as that observed in Cu_1Co_4 catalysts (Figure 7a), but the performance advantages of the ZrO_2-promoted architecture compared to that of the unpromoted and supported ones are nonetheless clear in all three bimetallic families regardless of the active metal pairing.

Similarly, by optimizing reaction conditions (Tables S15 and 16), a remarkable STY_{HA} of 279.0 mg_{HA} h^{-1} g_{cat}^{-1} (S_{HA} = 20.5%) and 345.3 mg_{HA} h^{-1} g_{cat}^{-1} (S_{HA} = 23.2%) were attained for Cu_1Fe_2@ZrO_2-10 and Co_1Fe_4@ZrO_2-10, respectively, for at least 350 h on stream (Figures S9 and S10).

In the context of existing m-FTS catalysts reported in the literature under comparable operating conditions (Tables S17), the best performing catalysts herein reported compare favorably in terms of both STY_{HA} and S_{HA} (Figure 7b).

Insights into the Nature and Role of ZrO_2. Since relatively low ZrO_2 contents in $M_{1\alpha}M_{2\beta}$@ZrO_2-γ catalysts were sufficient to significantly enhance catalytic performance beyond geometric effects, the Cu_1Co_4@ZrO_2-5 catalyst was first thoroughly characterized to explore electronic and interfacial effects associated with ZrO_2 in promoted Cu-Co catalysts, followed by an analogous extension to the Cu-Fe and Co-Fe families.

The first step was to visualize metal and ZrO_2 distributions and compare them with their unpromoted and supported counterparts (Figure 8). HAADF-STEM coupled with EDX mapping of used Cu_1Co_4@ZrO_2-5 samples (Figures 8b and S11) feature well-dispersed ZrO_2 ranging from clusters to larger islands up to several nanometers in size covering small, evenly distributed Cu and Co nanoparticles. These ZrO_2 regions are likely to be highly amorphous, owing to the absence of diffraction peaks pertaining to crystalline ZrO_2 polymorphs in the XRD profiles at all contents below 20 mol % (Figures S1 and S12). A high interfacial density between Cu and Co nanoparticles and ZrO_2 is also visible, in line with the structural promotion effect shown in Figure 4b. It is reasonable to think that this distribution, where ZrO_2 can act as a barrier phase between metal domains, may hinder sintering (Figure S13). Elemental maps also revealed that ZrO_2 addition enhances metal dispersion compared to that in the unpromoted case (Figures 8a and S14) and density of ZrO_2-metal interfacial sites compared to the supported system (Cu_1Co_4/ZrO_2-90, Figure 8c). Additionally, STEM-EDX

https://doi.org/10.1021/acscatal.3c02534
ACS Catal. 2023, 13, 9946−9959

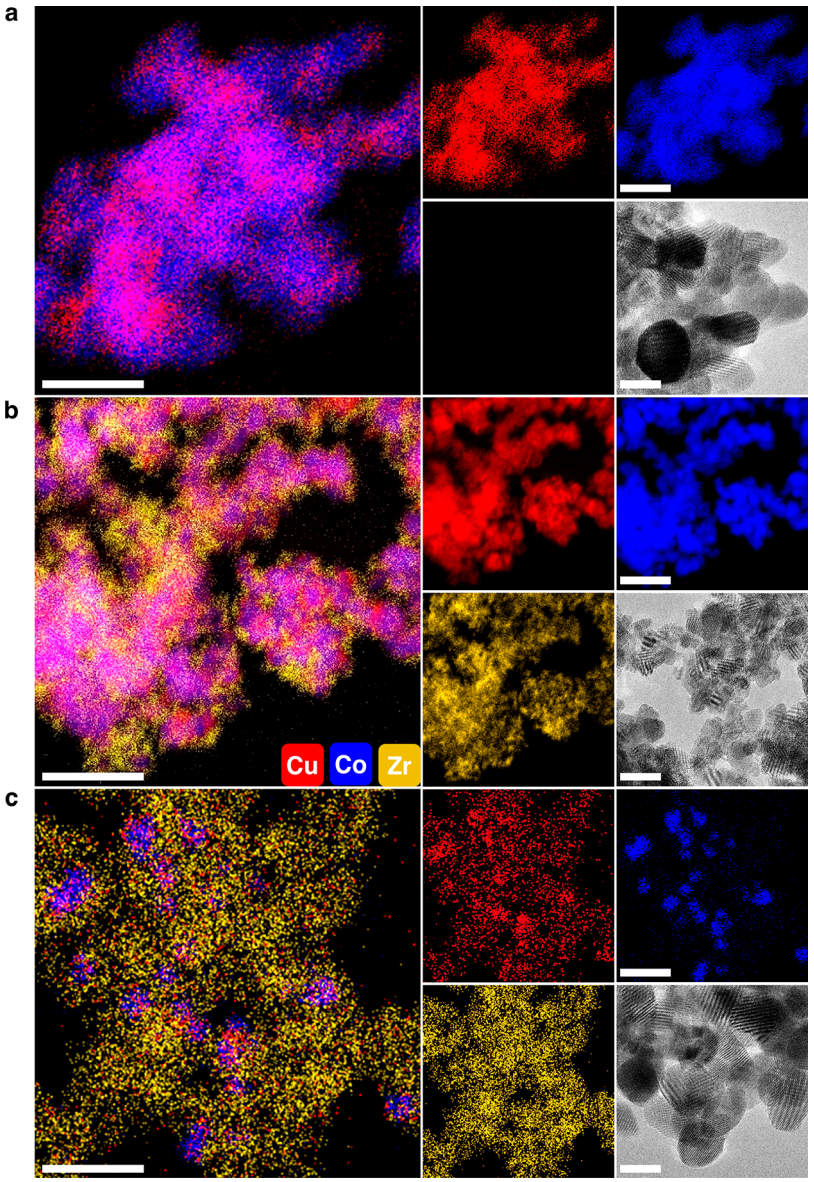

Figure 8. STEM-EDX elemental mapping and TEM images after reaction obtained from catalysts with α:β = 1:4 with varying ZrO_2 contents: (a) Cu_1Co_4, (b) ZrO_2-promoted Cu_1Co_4@ZrO_2-5, and (c) supported Cu_1Co_4/ZrO_2-90. Scale bars represent 50 nm for elemental maps and 20 nm for TEM images.

images further showed a much higher dispersion for Cu than for Co in the supported case, possibly due to different metal-ZrO_2 interaction strengths,[37] again leading to inferior proximity of intermetallic sites. Interestingly, for Cu_1Co_4@ZrO_2-90, both Cu and Co elements were highly dispersed on ZrO_2 and no visible particles were observed (Figure S15). However, the STY_{HA} of Cu_1Co_4@ZrO_2-90 was only half of Cu_1Co_4/ZrO_2-90 (Table S6), due to particle size effects critical in FTS-like reactions.[13] These initial observations suggested that the superior density and nature of Cu-Co-ZrO_2 interfacial sites in the ZrO_2-promoted architecture could be key features worthy of further investigation.

The well-studied role of ZrO_2 in hydrogenation catalysts recommended a careful evaluation of its effect on the interaction of catalysts with hydrogen.[38] The influence of γ in the response of Cu_1Co_4@ZrO_2-γ catalysts to H_2-TPR analyses was performed to evaluate copper and cobalt oxide reducibility (Figure 9; Figure S16 shows the H_2-TPR analysis for pure CuO and Co_3O_4 references). For γ = 0−20 mol %, increasing γ shifted metal oxide reduction peaks T_{peak} (CuO to metallic Cu, Figure 9a, Co_3O_4 to CoO and subsequently metallic Co, Figure 9b) toward lower temperatures, indicating more facile reduction in the presence of ZrO_2. This observation is aligned with the direct relation between γ and the alkane:alkene ratio observed in the product stream (Figure S17). These results suggest that ZrO_2 might influence the H* coverage and hydrogenation activity, phenomena similarly hypothesized for methanol synthesis.[39] Temperature-programmed H_2-D_2 exchange experiments[40] (Figure 10) further demonstrate the improved H_2 activation ability of Cu_1Co_4@ZrO_2-10 compared to Cu_1Co_4, with the exchange temperature of the former (onset of HD formation) occurring more than 20 K lower, signifying more facile H_2 and D_2 splitting and recombination. Noticeably, increasing γ from 20 mol % to beyond 50 mol % does not result in further reducibility changes (Figure 9d). Instead, new signals pointing to less facile

https://doi.org/10.1021/acscatal.3c02534
ACS Catal. 2023, 13, 9946−9959

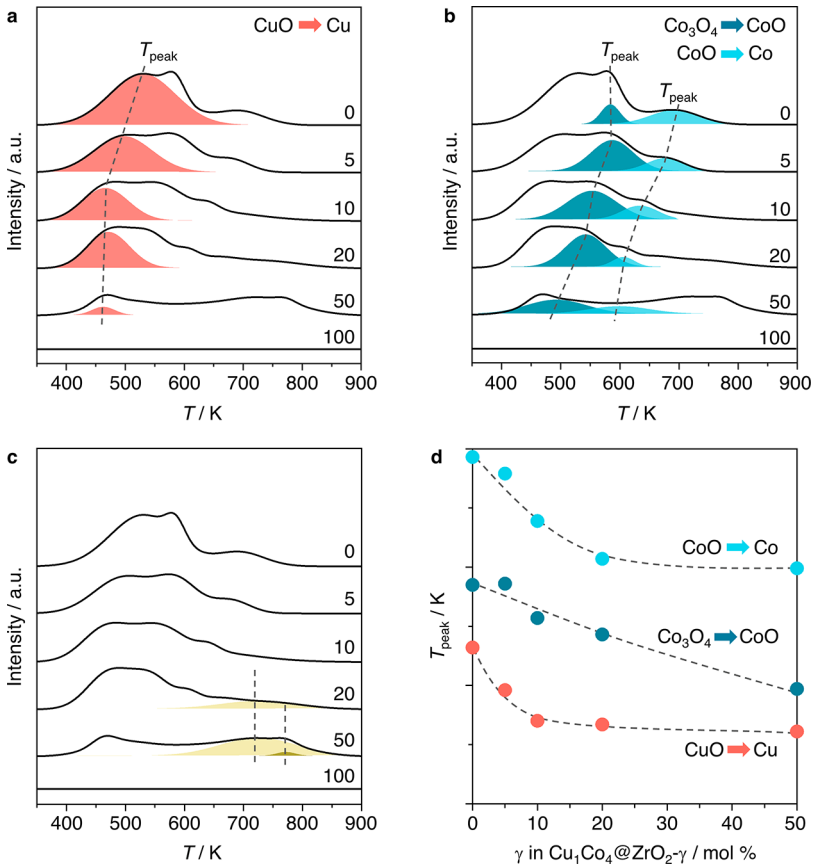

Figure 9. Influence of γ on the response to H_2-TPR analysis for Cu_1Co_4@ZrO_2-γ catalysts. Signals used to deconvolute experimental profiles correspond to the reduction of (a) Cu oxide; (b) Co oxides; and (c) additional Cu-Co-ZrO_2 oxidic phases. (d) Influence of γ on the phase reduction peak temperature, T_{peak}.

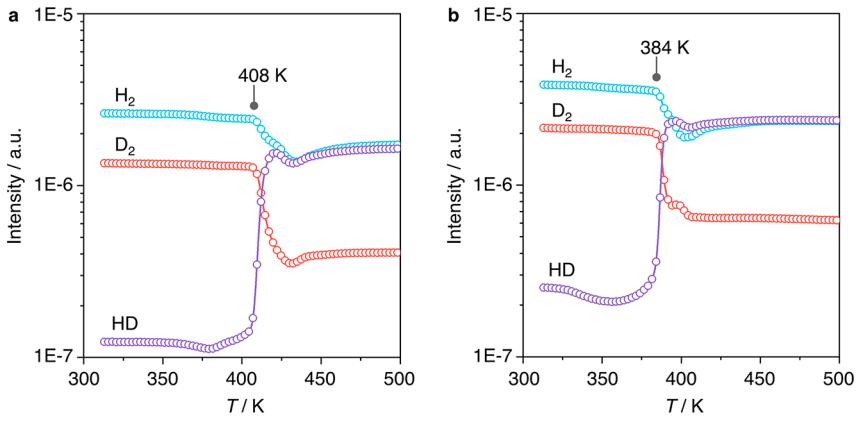

Figure 10. Temperature-programmed H_2-D_2 exchange profiles for (a) Cu_1Co_4 and (b) Cu_1Co_4@ZrO_2-10, with the exchange temperature (at the onset of HD formation) marked.

reduction of additional oxidic phases emerge (Figure 9c) that are tentatively associated with interfacial sites comprising Cu, Co, and larger and likely more crystalline ZrO_2 domains, where electron transfer between Cu/Co and ZrO_2 could lead to the reduction and formation of small Cu or Co particles stabilized by ZrO_2 as well as the generation of surface oxygen vacancies in ZrO_2.[37,41]

A step further, the analysis of chemical states disclosed unique properties of the ZrO_2-promoted catalyst architecture. Ex situ XPS analyses of the used Cu_1Co_4@ZrO_2-5, Cu_1Co_4, and Cu_1Co_4/ZrO_2-90 catalysts were performed to capture the main surface electronic features of these systems (Figure 11). Common features for all Cu_1Co_4-based catalysts can be found on the copper and carbon regions. Cu *LMM* spectra showed characteristic peaks at *BE* = 570.5 and 567.8 eV for Cu^{1+} and Cu^0 species, respectively, likely reflecting a partial surface reoxidation upon exposure to air after reaction for all samples. No signals attributed to Cu^{2+} were detected in the Cu 2*p* spectra (Figure S18). For C 1*s* spectra, the peak at 289.0 eV could be assigned to −COO or −C═O groups in organic acids or aldehydes[42] possibly arising from reaction intermediates remaining strongly bound to the catalyst surface.

https://doi.org/10.1021/acscatal.3c02534
ACS Catal. 2023, 13, 9946−9959

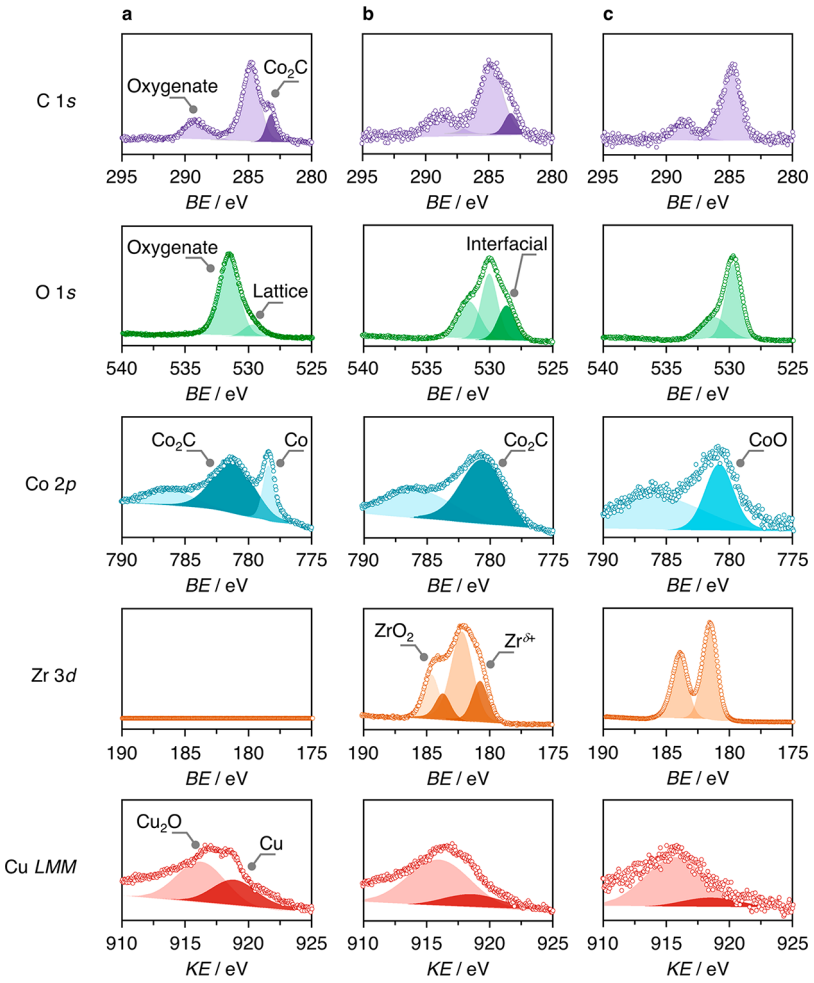

Figure 11. XPS spectra around indicated regions after reaction obtained from catalysts with α:β = 1:4 with varying ZrO_2 contents: (a) Cu_1Co_4, (b) ZrO_2-promoted Cu_1Co_4@ZrO_2-5, and (c) supported Cu_1Co_4/ZrO_2-90. Signals used to deconvolute experimental spectra correspond to indicated species.

More importantly, two notable features distinguish the ZrO_2-promoted catalyst from its unpromoted and supported counterparts. Deconvolution and assignment of the Co 2*p* signal of the Cu_1Co_4 catalyst (Figure 11a) showed three characteristic peaks around 786.7, 781.0, and 778.3 eV, which can be ascribed to satellite, Co^{2+}, and metallic Co species, respectively. Of the two possible assignments for the Co^{2+} species, CoO and Co_2C, the latter was deduced to be present, in line with the peak at around 283.2 eV of the C 1*s* spectrum assigned to Co_2C. XRD measurements of used Cu_1Co_4 catalysts (Figure S10) further show characteristic peaks pertaining to Co_2C without the presence of CoO. However, for the Cu_1Co_4@ZrO_2-5 catalyst, only satellites and Co_2C were detected and not metallic Co (Figure 11b), hinting that the presence of low contents of ZrO_2 promotes carbide formation from metallic Co (as metallic Co was the main phase observed for freshly reduced catalysts from Figures S4 and S19). Meanwhile, for the ZrO_2-supported Cu_1Co_4 catalyst, only CoO was observed (Figure 11c).

The second distinctive feature of the ZrO_2-promoted system is associated with metal−support interfaces. The deconvolution of the signal obtained in the Zr 3*d* region for the Cu_1Co_4@ZrO_2-5 catalyst (Figure 11b) necessitates the assignment of a secondary signal (*BE* = 180.6 eV) besides the one associated with the lattice Zr^{4+} (*BE* = 181.8 eV), that could be assigned to a lower oxidation state species (denoted $Zr^{\delta+}$) not present in the supported catalyst (Figure 11c).[28] This observation was matched in the O 1*s* spectrum, where an additional signal (*BE* = 528.6 eV) needed for deconvolution could be ascribed to polarized oxygen atoms in the vicinity of interfacial oxygen vacancies between ZrO_x and Cu or Co species. Based on this, surface ZrO_x species in the Cu_1Co_4@ZrO_2-5 catalyst are likely to be defective at its interface with metals and different from bulk ZrO_2 in supported catalysts. From the XPS results of the reduced catalyst (Figure S19), partial reduction to ZrO_x may occur during catalyst pretreatment in H_2. Since CO-TPD profiles (Figure S20) indicated more favorable CO adsorption on the ZrO_2-promoted catalyst than on the unpromoted and supported counterparts based on integral areas under the curves, we hypothesize that the high population of defects over the ZrO_x phase may also foster CO capture and activation.[28]

The General Promotional Effect of Zirconia. The newly obtained knowledge pertaining to the structural and electronic roles of ZrO_2 can be generalized to include the $Cu_\alpha Fe_\beta$@ZrO_2-γ and $Co_\alpha Fe_\beta$@ZrO_2-γ families. Similar structural motifs appear in the HAADF-STEM and TEM images of Cu_1Fe_2@ZrO_2-10 (Figures 12a and S21) and Co_1Fe_4@ZrO_2-10 (Figures 12b and S22), showing a common architecture with highly dispersed ZrO_2 in contact with small active metal

https://doi.org/10.1021/acscatal.3c02534
ACS Catal. 2023, 13, 9946−9959

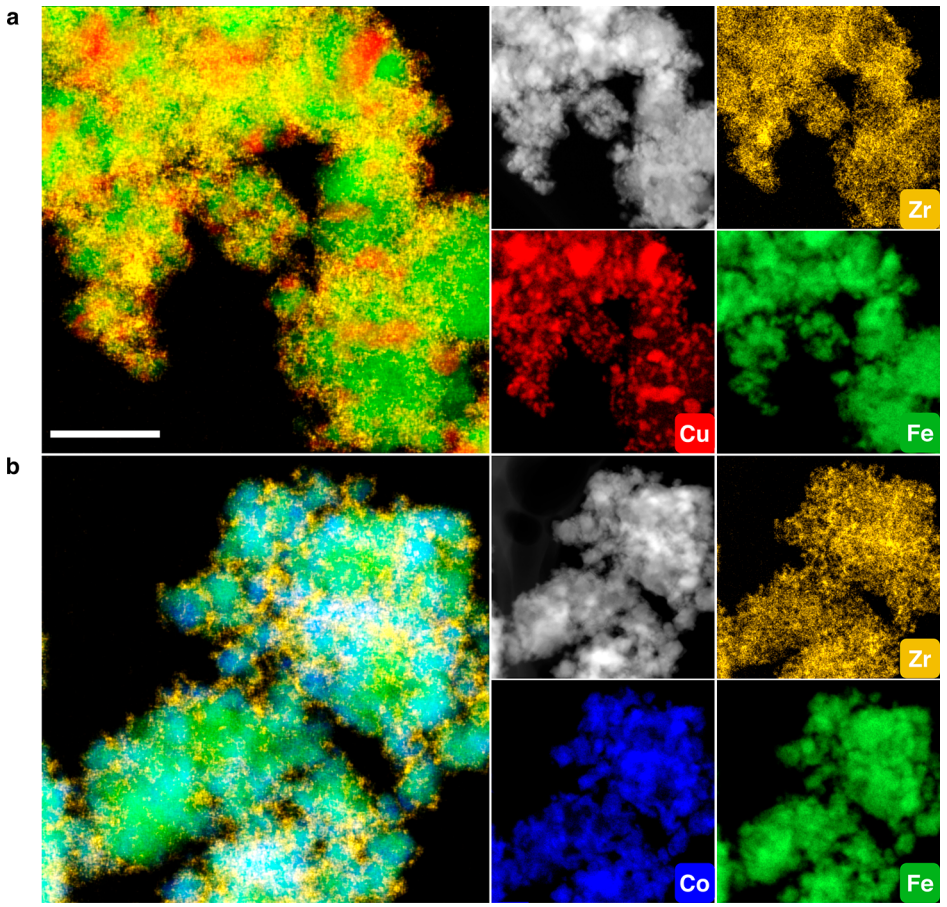

Figure 12. STEM-EDX elemental mapping and STEM images of (a) $Cu_1Fe_2@ZrO_2$-10 and (b) $Co_1Fe_4@ZrO_2$-10. Scale bars represent 50 nm in all images.

nanoparticles. Meanwhile, the presence of ZrO_2 reduced the particle sizes and crystallinity of the metal oxide precursors (Figures S23 and S24). Along with evidence of Co and/or Fe carbide formation (Figures 13a, S25 and S26), the defective nature of ZrO_2 in both cases is corroborated by the presence of the corresponding deconvoluted peaks in the XPS spectra (Figure 13b,c), this is notably implying that such a favorable feature of the oxide is not limited to a specific metallic combination with which it interacts but possibly a general property of zirconia in promoted catalysts. This may lead to similar behaviors in terms of reactant activation. As with $Cu_1Co_4@ZrO_2$-γ, the increase in iron oxide reducibility in H_2-TPR experiments on $Cu_1Fe_2@ZrO_2$-γ (Figures 13d and S27) and $Co_1Fe_4@ZrO_2$-γ (Figures 13e and S28) catalysts upon increasing γ hints at improved hydrogen activation in the presence of ZrO_2. The contrasting trends in CuO reducibility in $Cu_1Fe_2@ZrO_2$-γ and Co_3O_4 reducibility in $Co_1Fe_4@ZrO_2$-γ may originate from the differing nature of Cu and Co in interaction with Fe, being less favorable for the former leading to more apparent Cu segregation and lowered Cu-Fe interfacial area, while Co-Fe alloying is possible.

In contrast to the more commonly reported supported metal catalysts, the presence of low quantities of metal oxide on active metals is a shared characteristic among all of the families investigated. Rodriguez et al. initially introduced the term "inverse catalyst" for model systems exhibiting layers of metal oxides on flat metal surfaces.[25−27] Subsequently, this term has been extended to describe more realistic catalysts in the related water−gas shift and methanol synthesis reactions, among other applications.[28−30] However, the precise boundaries in terms of composition and physical or catalytic properties of this concept remain elusive, precluding a clear distinction from the established concept of promotion of bulk metal catalysts by metal oxides. In our view, the term "inverse catalyst" may appropriately describe the general architecture involving relatively low amounts of oxides dispersed on bulk metals, whereas the term "promoted" would imply enhanced performance relative to the oxide-free bulk metals. As such, all catalysts examined in Figure 3b exhibit an "inverse" architecture, but only CeO_2, Al_2O_3, or ZrO_2 would act as promoters.

The promotional effect of zirconia is a clear and common outcome and provides indirect insights on the resultant impact of various structural features on reactant activation (Figure 14). In the optimal catalysts containing up to 10 mol % of ZrO_2, defect-rich amorphous ZrO_2 in intimate contact with Cu-, Co-, and Fe-containing phases may promote H_2 activation at metal−support interfacial sites, enhancing surface H* coverage. The activation of CO, whether dissociative or nondissociative, may also be enhanced boosted by the more facile carbide formation.[43,44] A high density of interfacial sites between ZrO_2 domains and Co, Cu, or Fe with a low tendency to sinter may favor coupling of adsorbed intermediate species, increasing the rate of HA production. Deeper understanding of oxide-metal interactions will require accurate quantification of the density of metal-zirconia interfacial sites, assessing the unequal interactive nature and strength between Cu-ZrO_2, Co-

https://doi.org/10.1021/acscatal.3c02534
ACS Catal. 2023, 13, 9946−9959

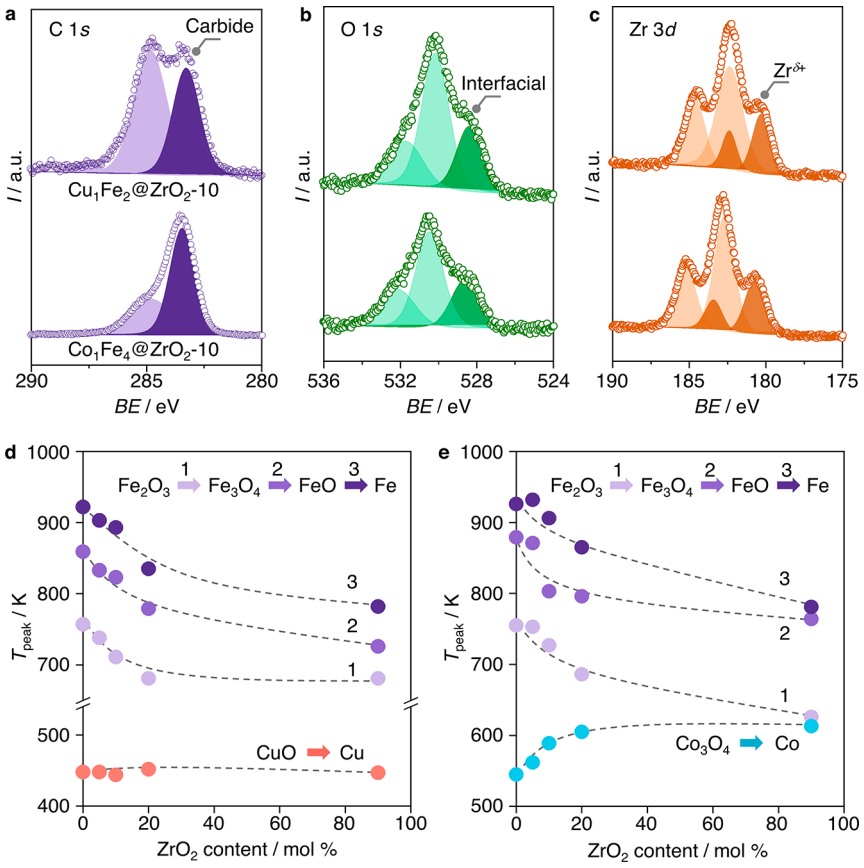

Figure 13. XPS spectra of used Cu_1Fe_2@ZrO_2-10 (above) and Co_1Fe_4@ZrO_2-10 samples (below) for (a) C 1*s*, (b) O 1*s* and (c) Zr 3*d* regions. Signals used to deconvolute experimental spectra correspond to indicated species. Influence of ZrO_2 content on the phase reduction peak temperature (T_{peak}) of (d) Cu_1Fe_2@ZrO_2-10 and (e) Co_1Fe_4@ZrO_2-10. The values of T_{peak} were extracted from the H_2-TPR results in Figures S25 and S26.

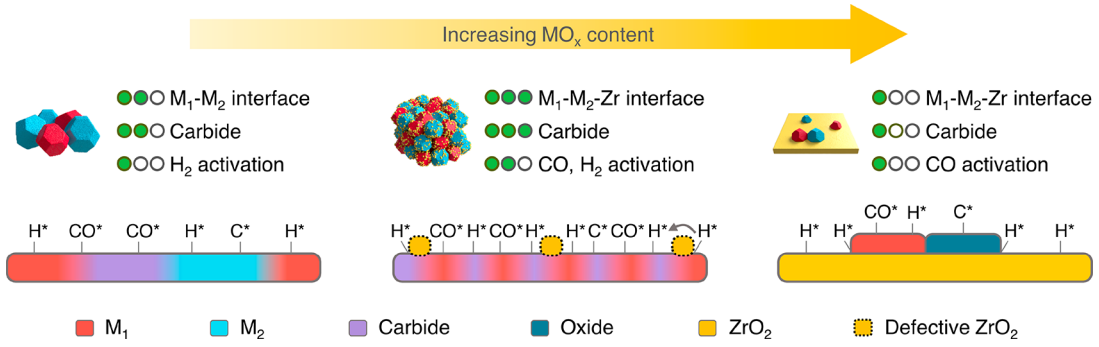

Figure 14. Overview of structural and catalytic features characteristic of zirconia-containing M_1M_2 catalysts for the analyzed architectures.

ZrO_2, and Fe-ZrO_2, and monitoring of catalyst surface dynamics using *operando* characterization techniques. While we have demonstrated the benefits of zirconia promotion as a general characteristic of all three families studied here, further work on the exploration of "inverse" architectures in HAS may reveal even more pronounced promotional effects.

CONCLUSIONS

This work presents the viability of small amounts of highly dispersed metal oxide on metal particles acting as activity and selectivity promoters in higher alcohol synthesis from syngas and shows its generality after revealing parallel features for Cu-Co, Cu-Fe, and Co-Fe systems. Upon developing a scalable synthetic route, this study revealed ZrO_2 displaying the largest potential over a variety of oxides. Volcano-like composition-performance trends applicable to all families identified 5−10 mol % ZrO_2 and different metal ratios (Cu:Co = 1:4, Cu:Fe = 1:2, Co:Fe = 1:4) as optimal compositions. These catalysts demonstrate superior performance; for instance, Cu_1Co_4@ZrO_2-5 achieved, respectively, two and five times higher HA productivity compared to unpromoted and supported counterparts with no sign of deactivation for at least 300 h on stream, while Co_1Fe_4@ZrO_2-10 showed the highest selectivity to HA of 31.8% and highest STY_{HA} of 345 mg_{HA} h^{-1} g_{cat}^{-1}, exhibiting the highest productivity reported under comparable conditions. Extensive characterization reveals unique catalytic properties associated with the architecture of ZrO_2-containing catalysts, primarily attributed to the multifaceted roles of

https://doi.org/10.1021/acscatal.3c02534
ACS Catal. 2023, 13, 9946−9959

zirconia. The zirconia promoter exhibits an amorphous and highly defective nature, leading to enhanced surface area, metal carbide formation, H_2 activation, and CO adsorption while also contributing to structural stability. These findings open up new pathways for future advancements in catalyst development for higher alcohol synthesis.

■ ASSOCIATED CONTENT

Data Availability Statement

The data relating to the figures and tables presented in this study are openly available in Zenodo under the DOI 10.5281/zenodo.7669540. Additional data underlying this study are available from the corresponding author upon reasonable request.

Supporting Information

The Supporting Information is available free of charge at https://pubs.acs.org/doi/10.1021/acscatal.3c02534.

Additional experimental characterization and evaluation data (PDF)

■ AUTHOR INFORMATION

Corresponding Author

Javier Pérez-Ramírez − *Institute of Chemical and Bioengineering, Department of Chemistry and Applied Biosciences, ETH Zurich, 8093 Zurich, Switzerland;* orcid.org/0000-0002-5805-7355; Email: jpr@chem.ethz.ch

Authors

Yuzhen Ge − *Institute of Chemical and Bioengineering, Department of Chemistry and Applied Biosciences, ETH Zurich, 8093 Zurich, Switzerland*

Tangsheng Zou − *Institute of Chemical and Bioengineering, Department of Chemistry and Applied Biosciences, ETH Zurich, 8093 Zurich, Switzerland*

Antonio J. Martín − *Institute of Chemical and Bioengineering, Department of Chemistry and Applied Biosciences, ETH Zurich, 8093 Zurich, Switzerland*

Complete contact information is available at: https://pubs.acs.org/10.1021/acscatal.3c02534

Notes

The authors declare no competing financial interest.

■ ACKNOWLEDGMENTS

This publication was financially supported by Sulzer Chemtech AG and NCCR Catalysis (grant number 180544), a National Centre of Competence in Research funded by the Swiss National Science Foundation. T.Z. thanks the Agency for Science, Technology and Research (A*STAR) Singapore for support through a graduate fellowship. The Scientific Center for Optical and Electron Microscopy (ScopeM) at ETH Zurich is thanked for access to their facilities. The authors are grateful to Dr. Frank Krumeich and Dario Faust Akl for acquiring HAADF-STEM-EDX and TEM images, Thaylan Pinheiro Araújo and Vera Giulimondi for XPS measurements, and Constance Ko for assistance with illustrations.

■ REFERENCES

(1) Luk, H. T.; Mondelli, C.; Curulla Ferré, D.; Stewart, J. A.; Pérez-Ramírez, J. Status and prospects in higher alcohols synthesis from syngas. *Chem. Soc. Rev.* **2017**, *46* (5), 1358−1426.

(2) Zeng, F.; Mebrahtu, C.; Xi, X.; Liao, L.; Ren, J.; Xie, J.; Heeres, H. J.; Palkovits, R. Catalysts design for higher alcohols synthesis by CO_2 hydrogenation: Trends and future perspectives. *Appl. Catal., B* **2021**, *291*, 120073.

(3) Xu, D.; Wang, Y.; Ding, M.; Hong, X.; Liu, G.; Tsang, S. C. E. Advances in higher alcohol synthesis from CO2 hydrogenation. *Chem.* **2021**, *7* (4), 849−881.

(4) Xiang, Y.; Barbosa, R.; Kruse, N. Higher alcohols through CO hydrogenation over CoCu catalysts: Influence of precursor activation. *ACS Catal.* **2014**, *4* (8), 2792−2800.

(5) Luk, H. T.; Novak, G.; Safonova, O. V.; Siol, S.; Stewart, J. A.; Curulla Ferré, D.; Mondelli, C.; Pérez-Ramírez, J. CO_2-promoted catalytic process forming higher alcohols with tunable nature at record productivity. *ChemCatChem.* **2020**, *12* (10), 2732−2744.

(6) Artz, J.; Muller, T. E.; Thenert, K.; Kleinekorte, J.; Meys, R.; Sternberg, A.; Bardow, A.; Leitner, W. Sustainable conversion of carbon dioxide: An integrated review of catalysis and life cycle assessment. *Chem. Rev.* **2018**, *118* (2), 434−504.

(7) Liu, G.; Yang, G.; Peng, X.; Wu, J.; Tsubaki, N. Recent advances in the routes and catalysts for ethanol synthesis from syngas. *Chem. Soc. Rev.* **2022**, *51* (13), 5606−5659.

(8) Li, Y.; Zhao, Z.; Lu, W.; Jiang, M.; Li, C.; Zhao, M.; Gong, L.; Wang, S.; Guo, L.; Lyu, Y.; et al. Highly selective conversion of syngas to higher oxygenates over tandem catalysts. *ACS Catal.* **2021**, *11* (24), 14791−14802.

(9) Chen, Y.; Ma, L.; Zhang, R.; Ye, R.; Liu, W.; Wei, J.; Ordomsky, V. V.; Liu, J. Carbon-supported Fe catalysts with well-defined active sites for highly selective alcohol production from Fischer−Tropsch synthesis. *Appl. Catal., B* **2022**, *312*, 121393.

(10) Zhao, Z.; Lu, W.; Yang, R.; Zhu, H.; Dong, W.; Sun, F.; Jiang, Z.; Lyu, Y.; Liu, T.; Du, H.; et al. Insight into the formation of Co@Co_2C catalysts for direct synthesis of higher alcohols and olefins from syngas. *ACS Catal.* **2018**, *8* (1), 228−241.

(11) Martin, O.; Mondelli, C.; Cervellino, A.; Ferri, D.; Curulla Ferre, D.; Pérez-Ramírez, J. Operando synchrotron X-ray powder diffraction and modulated-excitation infrared spectroscopy elucidate the CO_2 promotion on a commercial methanol synthesis catalyst. *Angew. Chem., Int. Ed.* **2016**, *55* (37), 11031−11036.

(12) Xiang, Y.; Chitry, V.; Liddicoat, P.; Felfer, P.; Cairney, J.; Ringer, S.; Kruse, N. Long-chain terminal alcohols through catalytic CO hydrogenation. *J. Am. Chem. Soc.* **2013**, *135* (19), 7114−7117.

(13) Bezemer, G. L.; Bitter, J. H.; Kuipers, H. P.; Oosterbeek, H.; Holewijn, J. E.; Xu, X.; Kapteijn, F.; van Dillen, A. J.; de Jong, K. P. Cobalt particle size effects in the Fischer−Tropsch reaction studied with carbon nanofiber supported catalysts. *J. Am. Chem. Soc.* **2006**, *128* (12), 3956−3964.

(14) Li, Y.; Gao, W.; Peng, M.; Zhang, J.; Sun, J.; Xu, Y.; Hong, S.; Liu, X.; Liu, X.; Wei, M.; et al. Interfacial Fe_5C_2-Cu catalysts toward low-pressure syngas conversion to long-chain alcohols. *Nat. Commun.* **2020**, *11* (1), 61.

(15) Prieto, G.; Beijer, S.; Smith, M. L.; He, M.; Au, Y.; Wang, Z.; Bruce, D. A.; deJong, K. P.; Spivey, J. J.; de Jongh, P. E. Design and synthesis of copper-cobalt catalysts for the selective conversion of synthesis gas to ethanol and higher alcohols. *Angew. Chem., Int. Ed.* **2014**, *126* (25), 6515−6519.

(16) Li, Z. S.; Luo, G. Y.; Chen, T.; Zeng, Z.; Guo, S. X.; Lv, J.; Huang, S. Y.; Wang, Y.; Ma, X. B. Bimetallic CoCu catalyst derived from in-situ grown Cu-ZIF-67 encapsulated inside KIT-6 for higher alcohol synthesis from syngas. *Fuel* **2020**, *278*, 118292.

(17) Xiang, Y.; Barbosa, R.; Li, X.; Kruse, N. Ternary cobalt-copper-niobium catalysts for the selective CO hydrogenation to higher alcohols. *ACS Catal.* **2015**, *5* (5), 2929−2934.

(18) Huang, C.; Ma, P.; Wang, R.; Li, W.; Wang, J.; Li, H.; Tan, Y.; Luo, L.; Li, X.; Bao, J. CuCo alloy nanonets derived from $CuCo_2O_4$ spinel oxides for higher alcohols synthesis from syngas. *Catal. Sci. Technol.* **2021**, *11* (23), 7617−7623.

(19) Bailliard-Letournel, R. M.; Gomez Cobo, A. J.; Mirodatos, C.; Primet, M.; Dalmon, J. A. About the nature of the Co-Cu interaction

in Co-based catalysts for higher alcohols synthesis. *Catal. Lett.* **1989**, *2* (3), 149−156.
(20) Turchanin, M. A.; Agraval, P. G.; Nikolaenko, I. V. Thermodynamics of alloys and phase equilibria in the copper-iron system. *J. Phase Equilib.* **2003**, *24* (4), 307−319.
(21) Xiao, K.; Bao, Z.; Qi, X.; Wang, X.; Zhong, L.; Fang, K.; Lin, M.; Sun, Y. Structural evolution of CuFe bimetallic nanoparticles for higher alcohol synthesis. *J. Mol. Catal. A: Chem.* **2013**, *378*, 319−325.
(22) Gong, K.; Wei, Y.; Lin, T.; Qi, X.; Sun, F.; Jiang, Z.; Zhong, L. Maximizing the interface of dual active sites to enhance higher oxygenate synthesis from syngas with high activity. *ACS Catal.* **2023**, *13* (7), 4533−4543.
(23) Wang, Z.; Spivey, J. J. Effect of ZrO_2, Al_2O_3 and La_2O_3 on cobalt-copper catalysts for higher alcohols synthesis. *Appl. Catal., A* **2015**, *507*, 75−81.
(24) Subramanian, N. D.; Gao, J.; Mo, X.; Goodwin, J. G., Jr; Torres, W.; Spivey, J. J. La and/or V oxide promoted Rh/SiO_2 catalysts: Effect of temperature, H_2/CO ratio, space velocity, and pressure on ethanol selectivity from syngas. *J. Catal.* **2010**, *272* (2), 204−209.
(25) Rodriguez, J. A.; Graciani, J.; Evans, J.; Park, J. B.; Yang, F.; Stacchiola, D.; Senanayake, S. D.; Ma, S.; Perez, M.; Liu, P.; et al. Water-gas shift reaction on a highly active inverse CeO_x/Cu(111) catalyst: unique role of ceria nanoparticles. *Angew. Chem., Int. Ed.* **2009**, *48* (43), 8047−8050.
(26) Senanayake, S. D.; Stacchiola, D.; Rodriguez, J. A. Unique properties of ceria nanoparticles supported on metals: novel inverse ceria/copper catalysts for CO oxidation and the water-gas shift reaction. *Acc. Chem. Res.* **2013**, *46* (8), 1702−1711.
(27) Kapiamba, K. F.; Otor, H. O.; Viamajala, S.; Alba-Rubio, A. C. Inverse oxide/metal catalysts for CO_2 hydrogenation to methanol. *Energy Fuels* **2022**, *36* (19), 11691−11711.
(28) Wu, C.; Lin, L.; Liu, J.; Zhang, J.; Zhang, F.; Zhou, T.; Rui, N.; Yao, S.; Deng, Y.; Yang, F.; et al. Inverse ZrO_2/Cu as a highly efficient methanol synthesis catalyst from CO_2 hydrogenation. *Nat. Commun.* **2020**, *11* (1), 5767.
(29) Boffa, A.; Lin, C.; Bell, A. T.; Somorjai, G. A. Promotion of CO and CO_2 hydrogenation over Rh by metal oxides: The influence of oxide lewis acidity and reducibility. *J. Catal.* **1994**, *149* (1), 149−158.
(30) Zou, T.; Araújo, T. P.; Krumeich, F.; Mondelli, C.; Pérez-Ramírez, J. ZnO-promoted inverse ZrO_2-Cu catalysts for CO_2-based methanol synthesis under mild conditions. *ACS Sustainable Chem. Eng.* **2022**, *10* (1), 81−90.
(31) Donia, A. M.; Dollimore, D. Preparation, identification and thermal investigation of solid solutions of cobalt-copper oxalates. *Thermochim. Acta* **1997**, *290* (1), 139−147.
(32) Luk, H. T.; Forster, T.; Mondelli, C.; Siol, S.; Curulla-Ferré, D.; Stewart, J. A.; Pérez-Ramírez, J. Carbon nanofibres-supported KCoMo catalysts for syngas conversion into higher alcohols. *Catal. Sci. Technol.* **2018**, *8* (1), 187−200.
(33) Luk, H. T.; Mondelli, C.; Mitchell, S.; Siol, S.; Stewart, J. A.; Curulla Ferré, D.; Pérez-Ramírez, J. Role of carbonaceous supports and potassium promoter on higher alcohols synthesis over copper-iron catalysts. *ACS Catal.* **2018**, *8* (10), 9604−9618.
(34) Khodakov, A. Y.; Chu, W.; Fongarland, P. Advances in the development of novel cobalt Fischer−Tropsch catalysts for synthesis of long-chain hydrocarbons and clean fuels. *Chem. Rev.* **2007**, *107* (5), 1692−1744.
(35) Su, J.; Zhang, Z.; Fu, D.; Liu, D.; Xu, X.-C.; Shi, B.; Wang, X.; Si, R.; Jiang, Z.; Xu, J.; et al. Higher alcohols synthesis from syngas over $CoCu/SiO_2$ catalysts: Dynamic structure and the role of Cu. *J. Catal.* **2016**, *336*, 94−106.
(36) Xiang, Y.; Kruse, N. Tuning the catalytic CO hydrogenation to straight- and long-chain aldehydes/alcohols and olefins/paraffins. *Nat. Commun.* **2016**, *7*, 13058.
(37) Zhao, H.; Yu, R.; Ma, S.; Xu, K.; Chen, Y.; Jiang, K.; Fang, Y.; Zhu, C.; Liu, X.; Tang, Y.; et al. The role of Cu_1-O_3 species in single-atom Cu/ZrO_2 catalyst for CO_2 hydrogenation. *Nat. Catal.* **2022**, *5* (9), 818−831.
(38) Li, K.; Chen, J. G. CO_2 hydrogenation to methanol over ZrO_2-containing catalysts: Insights into ZrO_2 induced synergy. *ACS Catal.* **2019**, *9* (9), 7840−7861.
(39) Jung, K.-D.; Bell, A. T. Role of hydrogen spillover in methanol synthesis over Cu/ZrO_2. *J. Catal.* **2000**, *193* (2), 207−223.
(40) Liu, J.; Lucci, F. R.; Yang, M.; Lee, S.; Marcinkowski, M. D.; Therrien, A. J.; Williams, C. T.; Sykes, E. C.; Flytzani-Stephanopoulos, M. Tackling CO poisoning with single-atom alloy catalysts. *J. Am. Chem. Soc.* **2016**, *138* (20), 6396−6399.
(41) Gong, N.; Zhang, T.; Tan, M.; Wang, L.; Yang, J.; Tan, L.; Yang, G.; Wu, P.; Wu, Y.; Tan, Y. Realizing and revealing complex isobutyl alcohol production over a simple Cu-ZrO_2 catalyst. *ACS Catal.* **2023**, *13* (6), 3563−3574.
(42) Mudiyanselage, K.; Burrell, A. K.; Senanayake, S. D.; Idriss, H. XPS and NEXAFS study of the reactions of acetic acid and acetaldehyde over UO_2(100) thin film. *Surf. Sci.* **2019**, *680*, 107−112.
(43) Wang, Z.; Kumar, N.; Spivey, J. J. Preparation and characterization of lanthanum-promoted cobalt−copper catalysts for the conversion of syngas to higher oxygenates: Formation of cobalt carbide. *J. Catal.* **2016**, *339*, 1−8.
(44) Lebarbier, V. M.; Mei, D.; Kim, D. H.; Andersen, A.; Male, J. L.; Holladay, J. E.; Rousseau, R.; Wang, Y. Effects of La_2O_3 on the mixed higher alcohols synthesis from syngas over Co catalysts: A combined theoretical and experimental study. *J. Phys. Chem. C* **2011**, *115* (35), 17440−17451.

https://doi.org/10.1021/acscatal.3c02534
ACS Catal. 2023, 13, 9946−9959